CrossMark

ORIGINAL PAPER

Bifurcations of vortex-induced vibrations of a fixed membrane wing at $Re \leq 1000$

Xu Sun · Shi-Zhao Wang · Jia-Zhong Zhang · Ze-Hua Ye

Abstract Vortex-induced vibrations (VIVs) of a fixed two-dimensional perimeter-reinforced (PR) membrane wing at $0 \leq \alpha$ Re (Reynolds number) ≤ 1000 and $0° \leq \alpha$ (angle of attack) $\leq 30°$ are investigated using fluid–structure interaction simulations. By employing very fine increments for Re and α, bifurcation boundaries of the dynamic response of the membrane wing in the Re–α plane are captured. With increase in Re and/or α, it is found that the VIV state of a fixed PR membrane wing will change progressively from static state to period 1 via a Hopf bifurcation and then from period 1 to multiple period and chaos via a succession of period-doubling bifurcations. The Hopf bifurcation is triggered by the shedding of the leading- and/or trailing-edge vortices, while the period-doubling bifurcations are induced by the appearance and evolution of the secondary vortices on the upper surface of the membrane wing at higher Re and α. With an increase in the structure rigidity or pre-strain, the overall responses of the membrane wing are not changed much in the Re–α plane except that the period 1 response near $700 \leq Re \leq 1000$ and $14° \leq \alpha \leq 16°$ is destroyed, due to the significant change of the shedding process of the leading-edge vortices. Moreover, it is also found that unsteady responses of the PR membrane wing at $\alpha = 0°$ can be suppressed by small pre-strain.

Keywords Membrane wing · Vortex-induced vibration · Numerical simulation · Bifurcation · Fluid–structure interaction

X. Sun (✉) · Z.-H. Ye
National Engineering Laboratory for Pipeline Safety/MOE
Key Laboratory of Petroleum Engineering, China
University of Petroleum-Beijing, Beijing 102249, China
e-mail: xsun@cup.edu.cn

S.-Z. Wang
The State Key Laboratory of Nonlinear Mechanics,
Institute of Mechanics, Chinese Academy of Sciences,
Beijing 100190, China

J.-Z. Zhang
School of Energy and Power Engineering, Xi'an Jiaotong
University, Xi'an 710049, China

List of symbols

α	Angle of attack of the membrane wing
c	Chord length of the membrane wing
C_d	Structural damping normalized by u_∞
$\bar{C}_L$	Mean lift coefficient
$\bar{C}_D$	Mean drag coefficient
δ_0	Membrane pre-strain
Δp	Pressure difference between the lower and upper surfaces of the membrane normalized by $\rho_\infty u_\infty^2$
Δt	Time step normalized by c/u_∞
ξ	Coordinate of the local coordinate system on the flexible membrane normalized by c
E	Elastic modulus of the membrane normalized by $\rho_\infty u_\infty^2$
f	Frequency normalized by u_∞/c

h	Membrane thickness normalized by c
L	Membrane length before deforming
L'	Membrane length before deforming normalized by c
L_S	Membrane length after deforming normalized by c
n_P	Total number of grid nodes in the flow domain
n_E	Total number of grid elements in the flow domain
n_M	Total number of grid elements on the flexible membrane
p	Pressure normalized by $\rho_\infty u_\infty^2$
Re	Reynolds number with respect to the chord c and velocity of the free stream u_∞
ρ_∞	Density of the incompressible flow
ρ_S	Membrane density per unit length normalized by ρ_∞
t	Time normalized by c/u_∞
T	Membrane tension normalized by $\rho_\infty u_\infty^2/c$
u_∞	Velocity component of the free stream in x direction
u_x, u_y	Velocity components of the flow field in x and y directions normalized by u_∞
v	Membrane velocity normalized by u_∞
x, y	Coordinate components of the flow domain normalized by c
z	Membrane displacement normalized by c

1 Introduction

With rapid development of micro air vehicles (MAVs), the membrane wing has attracted more and more attention in the past two decades. Unlike the conventional rigid wing, the membrane wing is flexible and allowed to deform and vibrate under the aerodynamic load, and the structure deformation and vibration in turn have a great influence on the flow field. For the membrane wing, the fluid–structure interaction (FSI) plays a very important role and contributes a lot to its superior aerodynamic performance in the low-Reynolds-number flow regime [1–5].

Generally speaking, FSI influences the aerodynamic performance of a fixed membrane wing in two ways: camber effect and vortex-induced vibration (VIV). When there is air flowing past a fixed membrane wing

at positive angles of attack, the flexible part of the wing will deflect to the lee side, under the pressure difference between the lower and upper surfaces, and form a mean camber. Because the flow-induced mean camber will make the wing more streamlined, a membrane wing usually has higher time-averaged lift, larger stall angle and better adaptability to the wind gust [6–11]. In addition, the flexible membrane will also vibrate near the mean camber when the angle of attack and/or Reynolds number are not too small, due to the perturbation of the shedding vortices on the upper surface. Such VIV could further improve the aerodynamic performance of the membrane wing. In the experiments of Rojratsirkul et al. [12–15] and numerical analyses of Gordnier [8] and Gordnier and Attar [9], it has been found that, for the fixed two-dimensional (2D) and low-aspect-ratio three-dimensional (3D) membrane wings, VIV could promote the roll-up of the separated shear layer and the formation of the large-scale vortices over the wing. As a result, a flexible membrane wing usually has higher time-averaged lift and larger stall angle compared with the rigid wing with the same mean camber.

For the membrane wing, the state of VIV has a great effect on its aerodynamic performance. With changes of flow and structure parameters such as the angle of attack, Reynolds number, pre-strain, rigidity and aspect ratio, various VIV states of the membrane wing have been observed in the previous studies. For the perimeter-reinforced (PR) membrane wing [2,6], Galvao et al. [16] found by experiments that, in the range of $-10° \leq \alpha \leq 50°$ and $3 \times 10^4 \leq Re \leq 1.2 \times 10^5$, the well-defined standing wave responses only appear near the points of fluid–structure resonance, and the harmonic order is an increasing function of the Reynolds number. Song et al. [7] conducted similar experiments using the same PR membrane model with larger aspect ratio. Apparent membrane vibrations were captured at all testing conditions, and it was also observed that the harmonic order of the standing wave response increases with the Reynolds number in the resonant region. Rojratsirkul et al. [12–14] investigated the unsteady FSIs of a 2D PR membrane wing. In their experiments, the angle of attack was changed from 0° to 30° and $Re = 53{,}100$, $79{,}700$ and $106{,}000$ were considered. With increase in the angle of attack, the bi-stable, static and unsteady responses were observed. In addition, it was also found that, with increase in the Reynolds number in the regime of unsteady response, the mode number of VIV is increased first at moderate angles

of attack, while then not changed when the angle of attack exceeds a critical value. Using a computational method with high fidelity, Gordnier [8] simulated the dynamic motion of the membrane wing model proposed by Rojratsirkul et al. [12–14] in the laminar flow with $Re = 2500$. With the changes of the angle of attack, Reynolds number, pre-strain and rigidity, the static, second-mode standing wave, third-mode standing wave and chaotic responses were observed. Subsequently, Rojratsirkul et al. [15] investigated experimentally the dynamic responses of a membrane wing with low aspect ratio in the flows with $Re = 24,300, 36,500$ and $48,700$. Under combined effects of the leading-edge and tip vortices, the membrane wing shows a mixture of chordwise and spanwise vibration modes at lower angles of attack and chordwise vibration mode with second order at higher angles of attack, respectively. Gordnier and Attar [9] simulated the dynamic response of an aspect ratio two-membrane wing at $Re = 24,300$. They also found that the chordwise second-mode structural response is dominant at moderate and high angles of attack. Using much finer increment, Sun et al. [17] reanalyzed the influence of the flow and structure parameters in the computational model of Gordnier [8]. It was found that, with increase in Reynolds number or angle of attack, the VIV of a 2D PR membrane wing will bifurcate first from static state to period via a Hopf bifurcation due to the shedding of the trailing-edge vortex (TEV) and then change suddenly from period to chaos due to the shedding of the leading-edge vortex (LEV). In the region of period 1 response, it was also observed that the vibration mode will decrease with the increase in the Reynolds number or angle of attack.

In previous studies, aerodynamic performance and VIV of the PR membrane wing at $Re = 10^3 \sim 10^5$ have been investigated widely. In nature, some insects such as chalcid wasp and fruit fly are usually flying at smaller Reynolds numbers ($Re \leq 10^3$) [4]. In such low-Reynolds-number flow regime, effect of air viscosity is more significant and usually leads to more unfavorable aerodynamic conditions for controllable flight. To design membrane-wing-based MAVs flying at $Re \leq 10^3$ in future, a system study of the aerodynamic performance and dynamic behavior of the membrane wing in this range of Reynolds number is very important. In Sun et al. [17], dynamic responses of a 2D PR membrane wing at $Re = 100 \sim 1000$ and $\alpha = 8°$ are computed. However, in this work the

angle of attack is fixed at $8°$ and only static response is captured. To obtain an overall understanding of the dynamic response of a membrane wing at $Re \leq 10^3$, more simulations involving moderate and high angles of attack should be carried out.

In this paper, VIVs of a fixed 2D PR membrane wing at $0° \leq \alpha \leq 30°$ and $0 < Re \leq 1000$ are studied using a well-validated finite element method (FEM) for FSI simulation in laminar flow regime. Bifurcation points of the dynamic response of the membrane wing and the corresponding changes in the flow field with respect to the angle of attack and Reynolds number are addressed specially. Moreover, effects of structure parameters including the rigidity and pre-strain are also analyzed. This paper could reveal the unique dynamic behaviors of the membrane wings in the low-Reynolds-number flows with $Re \leq 1000$.

2 Governing equations

Figure 1 shows the 2D PR membrane wing model proposed by Rojratsirkul et al. [12–14]. As seen in the figure, the membrane wing consists of a rectangular membrane sheet and two rigid mounts with streamlined shape, and the membrane sheet is glued to the two rigid mounts to form the pinned boundary conditions at the leading and trailing edges. The membrane sheet has a much larger length in span and is unconfined at the root and tip. Therefore, the flow field and deformation of the membrane wing are essentially 2D at low Reynolds numbers.

The flow is assumed to be incompressible and laminar at $0° \leq \alpha \leq 30°$ and $0 < Re \leq 1000$ and governed by the 2D Navier–Stokes equations, which can be expressed by
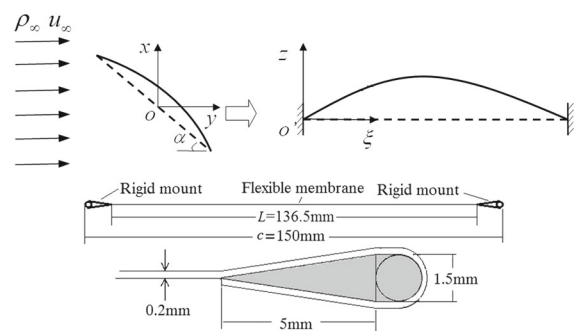

Fig. 1 Schematic of the uniform flow past a fixed 2D membrane wing [12–14]

$$\begin{cases} \frac{\partial u_x}{\partial x} + \frac{\partial u_y}{\partial y} = 0, \\ \frac{\partial u_x}{\partial t} + u_x \frac{\partial u_x}{\partial x} + u_y \frac{\partial u_x}{\partial y} = -\frac{\partial p}{\partial x} + \frac{1}{Re}\left(\frac{\partial^2 u_x}{\partial x^2} + \frac{\partial^2 u_x}{\partial y^2}\right), \\ \frac{\partial u_y}{\partial t} + u_x \frac{\partial u_y}{\partial x} + u_y \frac{\partial u_y}{\partial y} = -\frac{\partial p}{\partial y} + \frac{1}{Re}\left(\frac{\partial^2 u_y}{\partial x^2} + \frac{\partial^2 u_y}{\partial y^2}\right), \end{cases} \tag{1}$$

where the effect of the body force is not taken into account. The flexible membrane is supposed only driven by the pressure difference between the lower and upper surfaces, and the deformation is restricted in z direction, which is perpendicular to the chord of the wing, as seen in Fig. 1. A local coordinate system (ξ, z) with the origin O' located at the leading edge of the flexible membrane is utilized to describe the structure response. The nonlinear vibration equation proposed by Smith and Shyy [18,19] and Gordnier [8] is introduced as the governing equation of the structure, which can be written as

$$\begin{cases} \rho_S h \frac{\partial^2 z}{\partial t^2} + \rho_S C_d \frac{\partial z}{\partial t} - T\frac{\partial^2 z}{\partial \xi^2}\left[1 + \left(\frac{\partial z}{\partial \xi}\right)^2\right]^{-\frac{3}{2}} = \Delta p, \\ T = Eh\left(\delta_0 + \bar{\delta}\right), \bar{\delta} = \frac{L_S - L'}{L'}, \\ L_S = \int_0^{L'}\sqrt{1 + \left(\frac{\partial z}{\partial \xi}\right)^2}\,\mathrm{d}\xi. \end{cases} \tag{2}$$

3 Numerical method

A well-validated FSI solution procedure proposed in our previous studies [17,20,21] is employed. In this method, a modified characteristic-based split (CBS) finite element method for moving mesh [22,23] is combined with the segment spring analogy method [24] and dual-time stepping method [25] to form an implicit flow solver, the membrane vibration is solved implicitly by the Galerkin FEM and generalized α method [26,27], and the flow and structure solvers are coupled by the loosely coupled partitioned approach. The one-dimensional flexible membrane is divided equally by Hermite elements, while the flow domain is divided by unstructured triangular grids with linear shape functions for velocity and pressure. Moreover, the grid nodes of the structure and fluid are overlapping on the fluid–membrane interface, and the same computational time step is used for the flow and structure solvers. For the fluid–membrane interaction problems in laminar flow regime, this FSI solution procedure shows good accuracy and stability. More details about the numerical methods can be found in Zienkiewicz et al. [28],

Sun et al. [17,22,23] and Sun and Zhang [20,21,27] and will not be discussed here.

4 Results and discussions

4.1 Grid and time-step independence tests

Figure 2 illustrates the computational model of a fixed 2D PR membrane wing in laminar flow. As seen in the figure, the flow domain is defined as $-8c \leq x \leq 16c$ and $-8c \leq y \leq 8c$, the free-stream velocity is imposed on the inlet and two side boundaries, the pressure on the outlet is assumed to be zero, and the no-slip boundary condition is imposed on the wing surface. On the lower and upper surfaces of the flexible membrane, the flow and structure have the same displacement, velocity and stress. As a result, the flow boundaries corresponding to the two surfaces of the flexible membrane will be moved due to the structure vibration during the simulating process. Before studying the cases at $Re \leq 1000$, aerodynamic characteristics of the 2D PR membrane wing at $Re = 2500$, $E = 50{,}000$, $\rho_S = 589$, $C_d = 0$, $h = 0.001$ and $AOA = 8°$ are computed first to test the effects of grid density and time step. Table 1 displays the computed mean lift and drag coefficients of the membrane wing obtained from three meshes with three time steps. As seen in the table, numerical results from different grid densities and time steps are very close. Moreover, the mean lift coefficient computed by the proposed FSI scheme has a very good agreement with that reported by Gordnier [8]. Finally, Mesh_2 with $\Delta t = 0.01$ is employed to study the dynamic responses of the membrane wing at $Re \leq 1000$.

4.2 Dynamic responses in the Re-α plane

With the non-dimensional structural parameters fixed at $Eh = 100$, $\rho_S = 589$, $C_d = 0$, $h = 0.001$ and
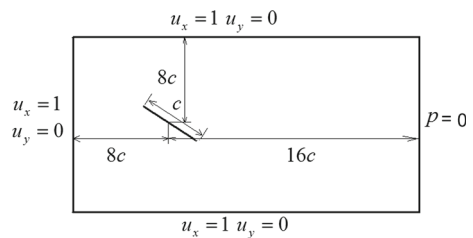

Fig. 2 Schematic of the solution domain and boundary conditions for the flow around a fixed PR membrane wing [17,21]

Table 1 Mean lift and drag coefficients of a fixed PR membrane wing at $Re = 2500$ and $AOA = 8°$

	n_M	n_P	n_E	Δt	$\bar{C}_L$	$\bar{C}_D$
				0.02	0.991	0.112
Mesh_1	60	5699	11,138	0.01	0.998	0.112
				0.005	1.0	0.112
				0.02	0.993	0.113
Mesh_2	80	7581	14,851	0.01	0.998	0.113
				0.005	0.995	0.113
				0.02	0.982	0.112
Mesh_3	100	10,103	19,850	0.01	1.0	0.113
				0.005	1.0	0.113
Gordnier [8]					1.05	
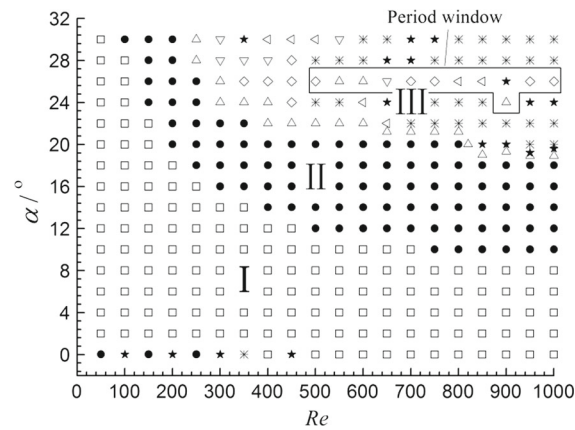
Fig. 3 Schematic of the vibration states at the membrane center at $Eh = 100$ and $\delta_0 = 0$. I represents the static region, II period 1 vibration region and III complicated region. Open square represents the static state, filled circle: period 1, open triangle: period 2, down open triangle: period 3, diamond: period 4, left triangle: multiple period (with period larger than four), star: quasiperiod, and asterisks: chaos

$\delta_0 = 0$, VIVs of the fixed 2D PR membrane wing (Fig. 1) at $0° \leq \alpha \leq 30°$ and $0 < Re \leq 1000$ are studied first. The increments of the angle of attack and Reynolds number are set respectively as $\triangle\alpha = 2°$ and $\triangle Re = 50$ in most regions of the $Re - \alpha$ plane. For local regions where the VIV state changes significantly, smaller $\triangle\alpha$ and $\triangle Re$ are utilized. As a result, more than 400 combinations of α and Re are computed to capture the bifurcation boundaries among different VIV states.

Figure 3 illustrates the dynamic responses at the membrane center in the $Re - \alpha$ plane of $0° \leq \alpha \leq 30°$ and $0 < Re \leq 1000$. As shown in the figure, various

VIV states are captured when the angle of attack and Reynolds number are changed in the $Re - \alpha$ plane considered. In general, the $Re - \alpha$ plane in Fig. 3 can be divided into three regions following the response of the membrane wing. At small α and/or Re, the response is in region I, where the membrane wing eventually reaches a static equilibrium state. In region II with moderate α and/or Re, however, the static equilibrium state is destroyed and the membrane wing is vibrating in the period 1 form. In region III with higher α and Re, the response becomes complicated and the vibrating states such as period 2, period 3, period 4, multiple period, quasiperiod and chaos are observed. With increase in α and/or Re, response of the membrane wing will first transfer from the static state in region I to period 1 in region II by Hopf bifurcation and then from the period 1 in region II to the more complicated states in region III by the period-doubling bifurcation. Moreover, the critical α (or Re) corresponding to the Hopf or period-doubling bifurcation is decreased gradually with the increase in Re (or α), which indicates that the stability of the membrane wing is decreased at higher α and/or Re. At high α and Re, the membrane wing is in a chaotic response at most points except the ones in the period window near $24° < \alpha < 28°$ and $500 \leq Re \leq 1000$, as shown in Fig. 3. In addition, the numerical results show that the membrane wing is unstable and might deform downward at $\alpha = 0°$ and $Re < 500$, which is consistent with that reported by Song et al. [7] and Rojratsirikul et al. [14].

4.2.1 Effect of Reynolds number

To show more clearly the effect of the Reynolds number on the dynamic response of the fixed 2D PR membrane, VIVs at $\alpha = 22°$ and $0 < Re \leq 1000$ are further analyzed. Figures 4 and 5 display the bifurcation diagram at the membrane center with respect to Re and the phase portraits and spectrograms at several representative points, respectively. As seen in Fig. 4, the membrane wing is at a static state and the deformation of the membrane center is decreased linearly when Re is increased in (0, 200). At $Re = 200$, however, the membrane wing begins to vibrate. As shown in Fig. 5a, the VIV at $Re = 200$ is period 1 and has a non-dimensional dominant frequency of 0.38 and a very small amplitude with an order of 10^{-3}. With further increase in Re in [200, 400), both of the amplitude and dominant frequency are increased and the influ-
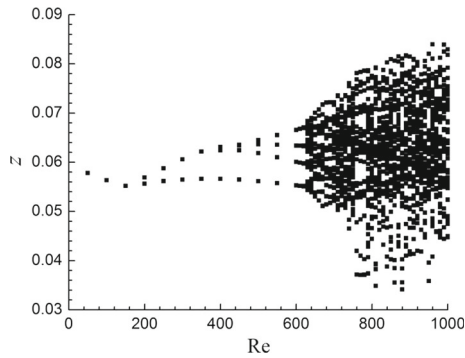
Fig. 4 Bifurcation diagram at the membrane center at $\alpha = 22°$ with respect to Re

ence of the higher harmonic frequency becomes more significant. Then, the VIV state is changed from period 1 to period 2 at $Re = 400$. As shown in Figs. 4 and 5b, the number of branches in the bifurcation diagram is increased from 2 to 4 and a cusp appears in the phase portrait at $Re = 400$. When Re is further increased from 400 to 620, the amplitude at the membrane center is also increased, and the period 2 characteristics become more and more evident, as seen in Figs. 4 and 5c. Moreover, the higher frequency component begins to dominate the vibration near $Re = 600$. Then, the response of the membrane wing is changed progressively from period 2 to multiple period and chaos in $Re \in [620,710]$ via a succession of period-doubling bifurcations. As displayed in Fig. 5d, the VIV state at $Re = 650$ has turned to multiple period with more harmonic frequencies appearing in the spectrogram. At $Re = 710$, the chaotic response occurs and many irrational frequency components can be observed in the spectrogram in Fig. 5e. Finally, the vibrating amplitude of the membrane wing at $\alpha = 22°$ is amplified gradually, but the chaotic response is not improved with further increase in Re from 710 to 1000, as shown in Fig. 4.

To better understand the transition process of the VIV state of the fixed membrane wing at $\alpha = 22°$ and $0 < Re \le 1000$, evolution of the flow field with respect to the Reynolds number is studied. Figure 6 shows the transient streamlines around the wing at different Reynolds numbers. As seen in Fig. 6a, there exist a LEV and a TEV on the upper surface of the membrane wing at $\alpha = 22°$ and $Re < 200$. Because the flow is steady and both of the LEV and TEV are not shed, the membrane wing is also in a static state. At $Re = 200$, however, the LEV and TEV begin to shed alternately

and periodically as seen in Fig. 6b, which results in the period 1 response of the membrane wing in Fig. 5a. When Re is increased up to 350, the large-scale LEV is split into two smaller ones during the shedding process, as shown in Fig. 6c. However, this change in flow domain does not affect much the VIV state of the membrane wing. At $Re = 400$, a small-scale secondary vortex appears near the center of the upper surface at some time instants in Fig. 6d. Because the secondary vortex will separate the large-scale LEVs from the wing surface and increase the local surface pressure, a small perturbation is introduced into the periodic fluid load at these time instants. As a result, the symmetry of the phase portrait is destroyed and the VIV is changed from period 1 to period 2 as shown in Fig. 5b. Then, this secondary vortex is enlarged slightly when Re is increased from 400 to 620. However, because the flow topology is nearly unchanged, the period 2 state is not changed as well. When the Reynolds number is further increased in $Re \in [620,710)$, the duration time as well as the effect of the secondary vortex is further increased as seen in Fig. 6f, which triggers the successive period-doubling bifurcations. In $Re \in [620,710)$, the main vortices are still attached to the wing surface, and thus the periodic characteristic of the response is maintained in this process. At $Re = 710$, the shedding LEVs begin to depart from the wing surface as shown in Fig. 6g. In this case, the large-scale LEVs are not always interacting directly with the membrane, which makes the fluid load as well as the dynamic response of the membrane wing more irregular, as shown in Fig. 5e. Finally, when Re is further increased in [710,1000], the large-scale LEVs are broken into more smaller ones and more secondary vortices appear, as shown in Fig. 6h. As a result, the chaotic response is not improved much in this Re range.

4.2.2 Effect of angle of attack

Effect of the angle of attack on the dynamic response of the fixed 2D PR membrane wing in Fig. 1 is investigated by fixing Re at 600 and changing α from 0° to 30°. The bifurcation diagram at the membrane center with respect to α and the phase portraits and spectrograms at several representative angles of attack are displayed respectively in Figs. 7 and 8. Comparing Fig. 7 with Fig. 4, it can be found that the variation trend of the VIV state with respect to α has an overall similarity with that with respect to Re. As shown in Fig. 7, the

Fig. 5 Phase portraits and spectrograms at $\alpha = 22°$ and different Reynolds numbers: **a** $Re = 200$; **b** $Re = 400$; **c** $Re = 600$; **d** $Re = 650$; **e** $Re = 710$
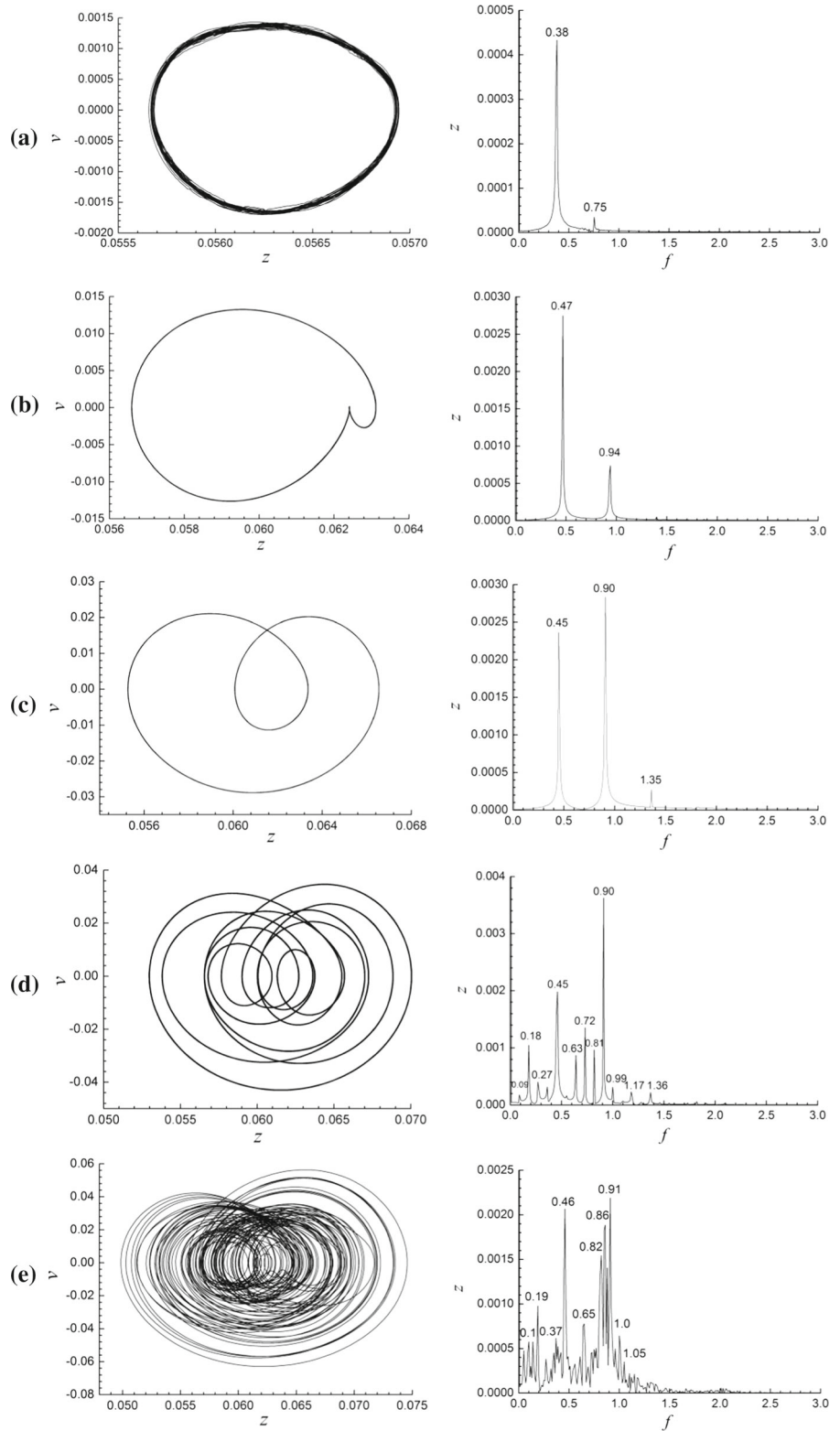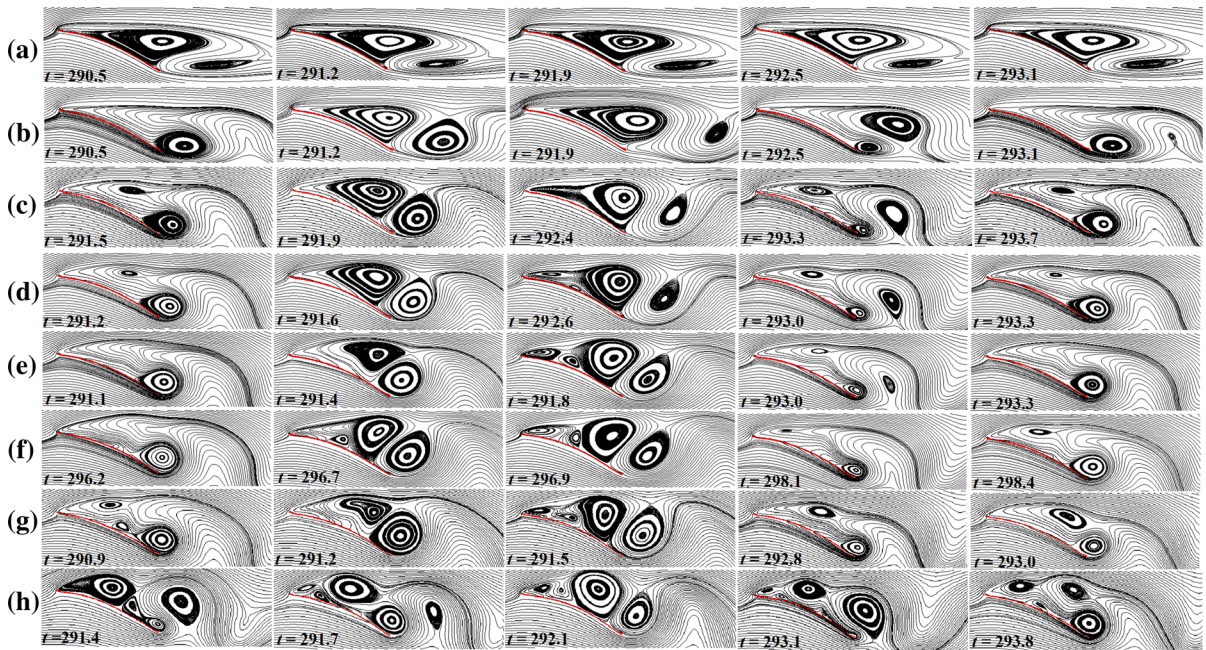
Fig. 6 Transient streamlines around a fixed PR membrane wing at $\alpha = 22°$: **a** $Re = 150$; **b** $Re = 200$; **c** $Re = 350$; **d** $Re = 400$; **e** $Re = 600$; **f** $Re = 650$; **g** $Re = 710$; **h** $Re = 1000$
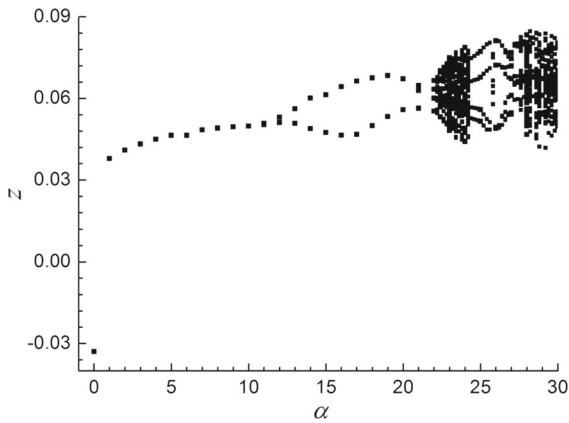

Fig. 7 Bifurcation diagram of the membrane center with respect to α at Re = 600

membrane wing is at a static equilibrium state at $\alpha < 11°$. In particular, the fluid–membrane system is found bi-stable and having two stable states near $\alpha = 0°$. The deflection of the membrane wing is downward at $\alpha = 0°$, but upward at $\alpha = 1°$, which results in an abrupt jump of the non-dimensional displacement from -0.033 to 0.0378 at the membrane center, as shown in Fig. 7. At $\alpha = 11°$, the response turns to period 1 with a frequency of 0.8 and an amplitude about $4 \times$

10^{-4}, as seen in Figs. 7 and 8a. In $\alpha \in [11°, 21°)$, the period 1 response is not changed, although the vibrating amplitude is first increased in $\alpha \in [11°, 17°]$ and then decreased in $\alpha \in [17°, 21°]$. However, the dominant frequency is decreased gradually and the effect of the harmonic frequency becomes more significant at higher α, as shown in Fig. 8a, b. Near $\alpha = 21°$, the amplitude of the harmonic frequency is further increased and the phase portrait is changed from period 1 to period 2, as shown in Fig. 8c. Then, the period 2 vibrating amplitude is increased slightly in $\alpha \in [21°, 22°]$. With further increase in α from 22° to 22.4° and 24.2°, the response of the membrane wing is changed progressively from period 2 to multiple period and chaos via a succession of period-doubling bifurcations, as seen in Figs. 7, 8d, e. Different from the bifurcation process with respect to Re as seen in Fig. 4, an apparent period window is observed in the bifurcation diagram with respect to α. As seen in Figs. 7 and 8f, the response of the membrane wing turns back to period 2 when α is increased slightly from 24.2° to 24.4°. It seems that the fluid–membrane system has jumped suddenly from the unstable state at 24.2° to a stable periodic state at $\alpha = 24.4°$, which is similar with that observed in our previous study when uniformly distributed periodic load is imposed on the same wing model [27]. When the angle of attack is

Fig. 8 Phase portraits and spectrograms at Re = 600 : **a** $\alpha = 11°$; **b** $\alpha = 20°$; **c** $\alpha = 21°$; **d** $\alpha = 22.4°$; **e** $\alpha = 24.2°$; **f** $\alpha = 24.4°$; **g** $\alpha = 26.6°$; **h** $\alpha = 27.4°$; **i** $\alpha = 28°$
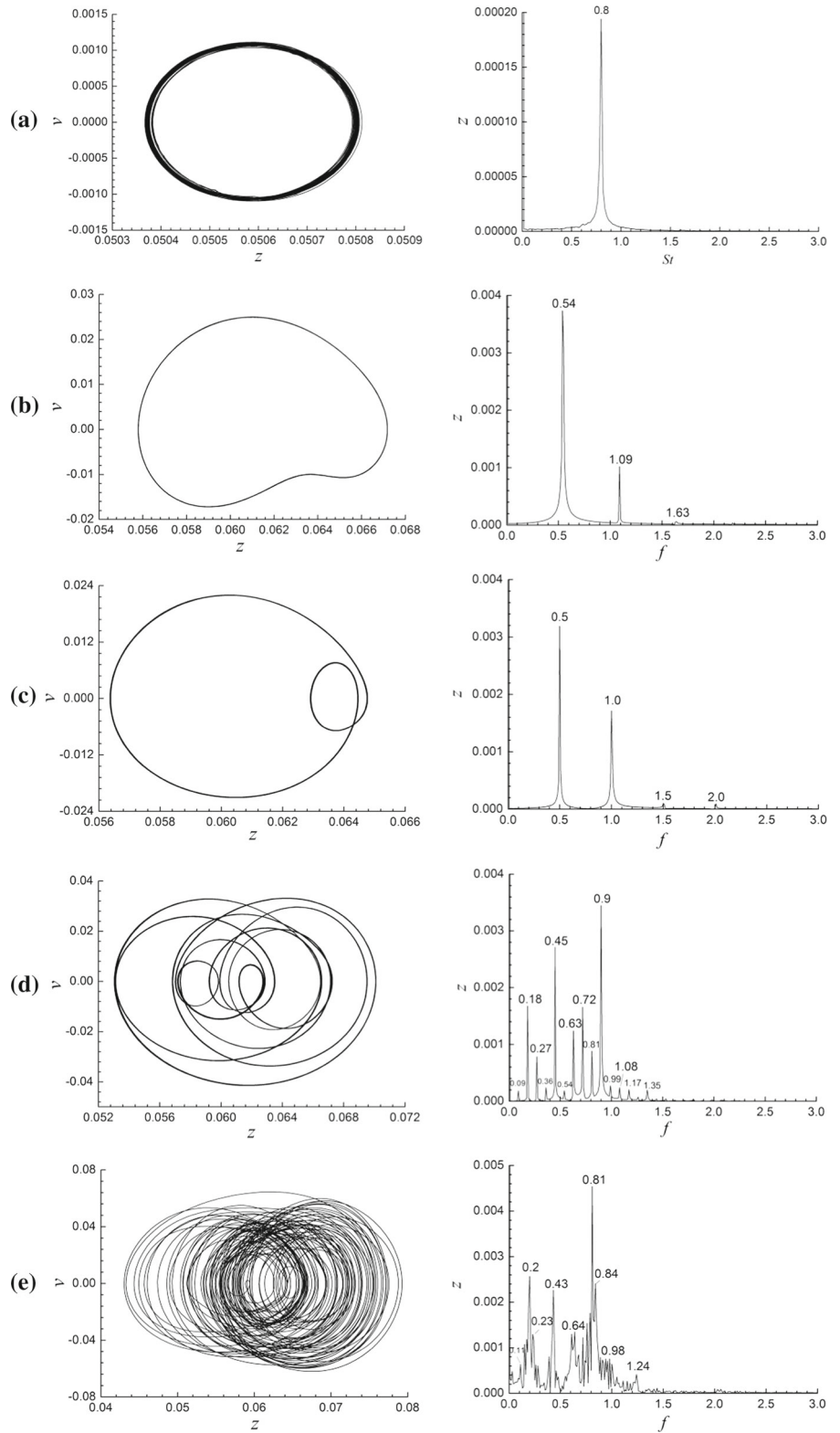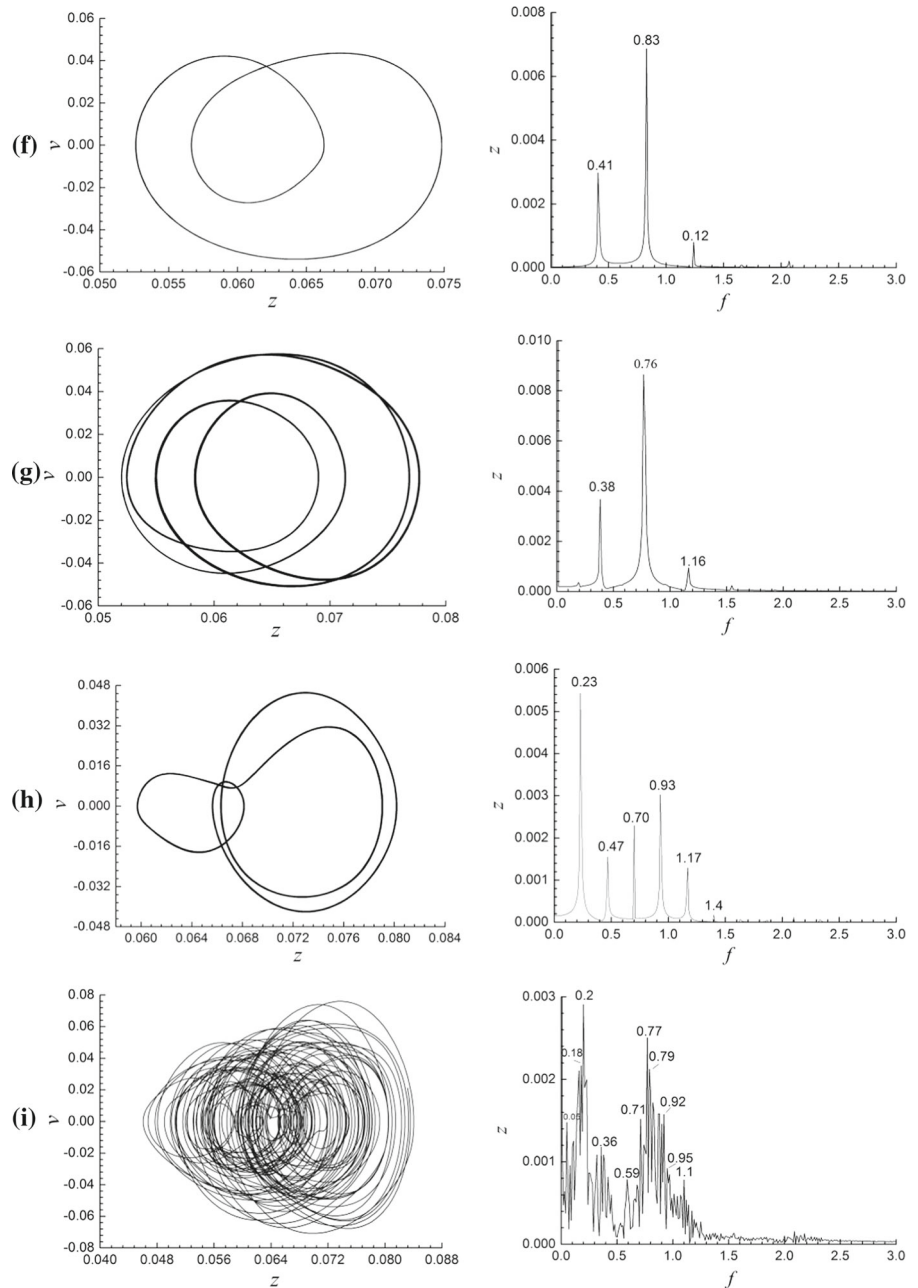
Fig. 8 continued

increased in the period window with $\alpha \in [24.2, 28)$, the period 2 vibrating state first turns to period 4 at $\alpha = 26.6°$ and then to period 3 at $\alpha = 27.4°$, as shown in Fig. 8g, h. Finally, the VIV state of the membrane wing turns back to chaos near $\alpha = 28°$ as shown in Fig. 8i.

Figure 9 displays the transient streamlines near the membrane wing at $Re = 600$ and different angles of attack. As seen in Fig. 9a, the flow is steady and there is a pair of small-scale vortices at the trailing edge of the membrane wing at $\alpha < 11°$. At $\alpha = 11°$, however, the TEVs begin to shed and result in the period 1
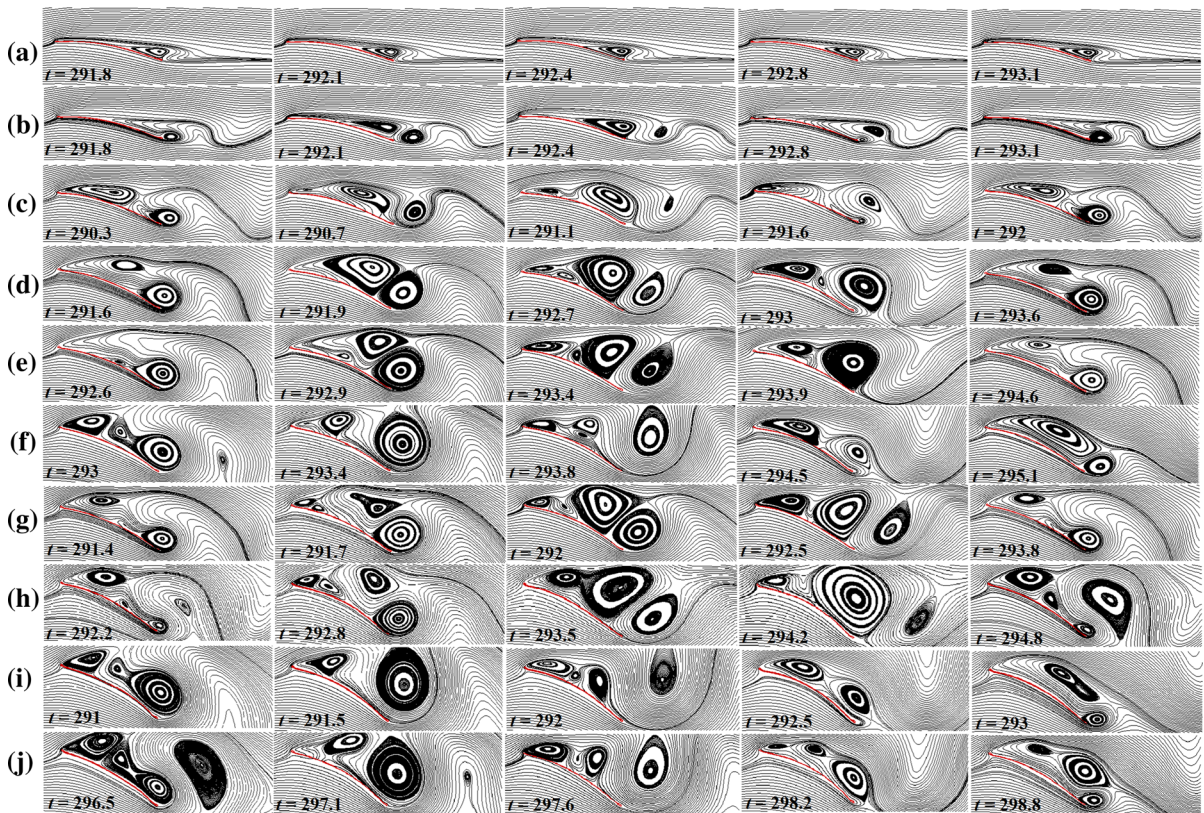
Fig. 9 Transient streamlines around the membrane wing at $Re = 600$: **a** $\alpha = 10°$; **b** $\alpha = 11°$; **c** $\alpha = 17°$; **d** $\alpha = 21°$; **e** $\alpha = 22.4°$; **f** $\alpha = 24.2°$; **g** $\alpha = 24.4°$; **h** $\alpha = 26.6°$; **i** $\alpha = 27.4°$; **j** $\alpha = 28°$

response of the membrane wing, as shown in Figs. 8a and 9b. Because only part of the membrane wing near the trailing edge is perturbed by the shedding TEVs, the vibrating amplitude is very small at $\alpha = 11°$. When α is increased from 11° to 17°, the scale of the TEVs is increased and the separation point of one of the TEVs is moved continuously to the leading edge, as seen in Fig. 9b, c, which results in linear increase in the vibrating amplitude in $\alpha \in [11°, 17°]$. At $\alpha = 17°$, the LEV begins to shed and play a more important role in the response of the membrane wing, as shown in Fig. 9c. In our previous studies [17,21] on the dynamic response the same membrane wing at $Re = 10^3 \sim 10^4$, we found that the shedding of the LEV will form a chain of vortices on the membrane upper surface, which will further result in the chaotic response. At $\alpha = 17°$ and $Re = 600$ studied here, however, the shedding of the LEV does not change the vibrating state of the membrane wing, although it decreases the VIV amplitude in $\alpha \in [17°, 21°]$, as shown in Fig. 7. At $\alpha = 21°$,

a secondary vortex appears at some time instants in Fig. 9d and once again triggers the transition of the VIV state from period 1 to period 2. Then, both of the strength and duration time of this secondary vortex are increased in $\alpha \in [22°, 24.2°)$. As a result, the response of the membrane wing further bifurcates progressively from period 2 to multiple period. At $\alpha = 24.2°$, the shed LEVs are split into more small-scale vortices as seen in Fig. 9f. In this case, the fluid load on the membrane wing becomes more complicated, which results in the chaotic response of the membrane wing. When α is increased slightly from 24.2° to 24.4°, however, the flow is stabilized and the breakdown of the shedding LEVs disappears in Fig. 9g. As a result, the chaotic VIV state is also stabilized and changed back to period 2. At $\alpha = 26.6°$, the effect of the secondary vortex becomes significant again and changes the VIV state from period 2 to period 4, as seen in Figs. 8g and 9h. At $\alpha = 27.4°$, a vortex shedding process similar with that in Fig. 9f is observed in Fig. 9i and it causes the
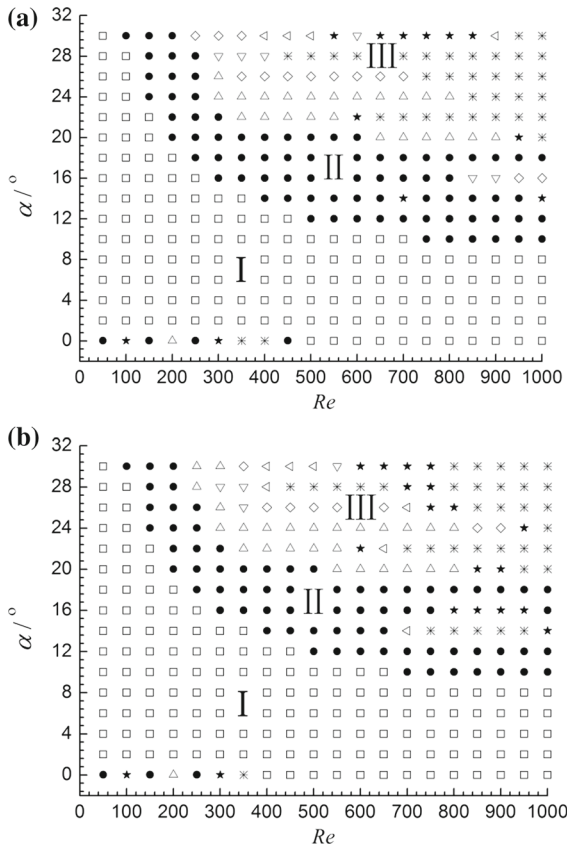
Fig. 10 Schematic of the vibration states at the membrane center at $\delta_0 = 0$ and different rigidities: **a** $Eh = 150$; **b** $Eh = 200$. I represents the static region, II period 1 vibrating region, and III complicated region. Square represents the static state, filled circle: period 1, open triangle: period 2, down triangle: period 3, diamond: period 4, left triangle: multiple period (with period larger than four), star: quasiperiod, and asterisks: chaos

period 3 response of the membrane wing. Finally, the shed LEVs begin to depart from the membrane upper surface near $\alpha = 28°$ as shown in Fig. 9j, which once again leads to the chaotic response of the membrane wing.

4.3 Effect of the membrane rigidity

To investigate the effect of the membrane rigidity (Eh), dynamic responses of the fixed 2D PR membrane wing at $Eh = 150$ and 200 are computed. For each Eh, the ranges and increments of α and Re are taken as $0° \leq \alpha \leq 30°$ and $\triangle\alpha = 2°$, $0 < Re \leq 1000$ and $\triangle Re = 50$, respectively. Figure 10 illustrates

the dynamic responses at the membrane center in the $Re - \alpha$ plane. Comparing Fig. 10 with Fig. 3, it can be found that, with the increase in the membrane rigidity, the region I with static response is not changed much, while the region III with complicated response is enlarged slightly. In addition, when Eh is increased from 100 to 150 and 200, the VIV state of most points in $700 \leq Re \leq 1000$ and $14° \leq \alpha \leq 16°$ is changed significantly. In Fig. 11, phase portraits and spectrograms at $Re = 900$, $\alpha = 16°$ and $Eh = 100$, 150 and 200 are presented to show more clearly this change. As seen in Fig. 11, the VIV state of the membrane center is period 1 at $Eh = 100$, period 3 at Eh=150 and quasiperiod at $Eh = 200$, respectively. Figure 12 displays the transient streamlines around the membrane wing at $Re = 900$, $\alpha = 16°$ and $Eh = 100$, 150 and 200. As shown in the figures, the shedding process of the LEVs has been changed significantly with the increase in Eh, due to the decrease in the mean camber of the membrane when Eh is increased from 100 to 150 and 200. At $Eh = 100$, the large-scale LEV is split into two or three small vortices in the shedding process, as shown in Fig. 12a. Because these small vortices are always very close to each other and interact with the membrane as one large-scale vortex, dynamic response of the membrane wing is still in the form of period 1. At $Eh = 150$ and 200, however, the secondary vortices are separated with each other and interact independently with the membrane, as shown in Fig. 12b, c. Under their combined perturbation, the period 1 state is destroyed and changed to period 3 and quasiperiod at $Eh = 150$ and 200, respectively, as seen in Fig. 11b, c.

4.4 Effect of the membrane pre-strain

To investigate the effect of the membrane pre-strain, dynamic responses of the fixed 2D PR membrane wing at $Eh = 100$ and $\delta_0 = 0.01$ and 0.02 are further computed. For each δ_0, the ranges and increments of α and Re are also taken as $0° \leq \alpha \leq 30°$ and $\triangle\alpha = 2°$, $0 < Re \leq 1000$ and $\triangle Re = 50$, respectively. In Fig. 13, dynamic responses at the membrane center at $\delta_0 = 0.01$ and 0.02 are illustrated in the $Re - \alpha$ plane. Comparing Fig. 3 with Fig. 13, it can be found that the pre-strain mainly affects the dynamic response of the membrane wing in two ways. First, when 1 or 2% pre-strain is imposed on the flexible membrane, all of the

Fig. 11 Phase portraits and spectrograms at $Re = 900$, $\alpha = 16°$ and $\delta_0 = 0$: **a** $Eh = 100$; **b** $Eh = 150$; **c** $Eh = 200$
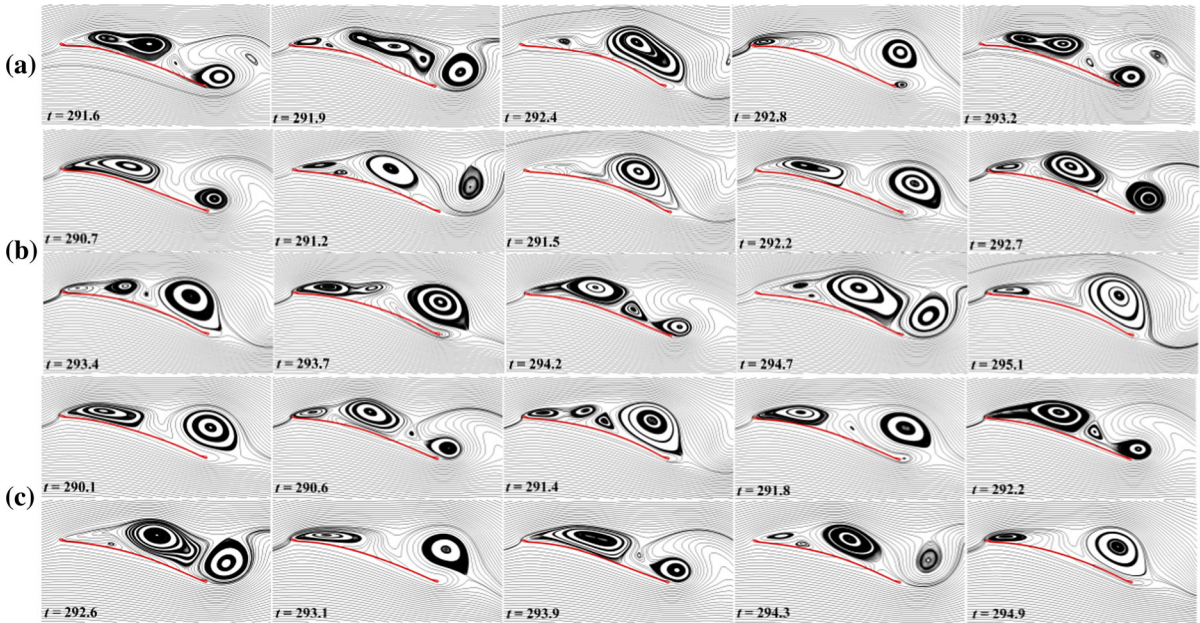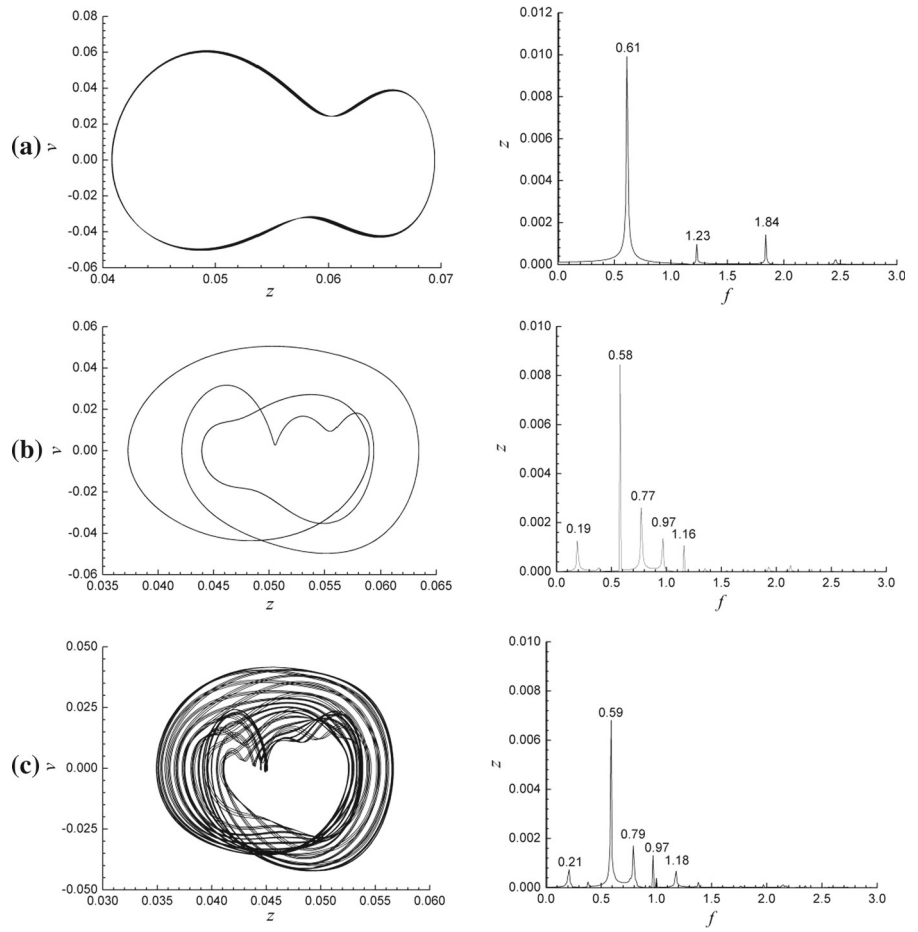

Fig. 12 Transient streamlines around the membrane wing at $Re = 900$, $\alpha = 16°$ and $\delta_0 = 0$: **a** $Eh = 100$; **b** $Eh = 150$; **c** $Eh = 200$
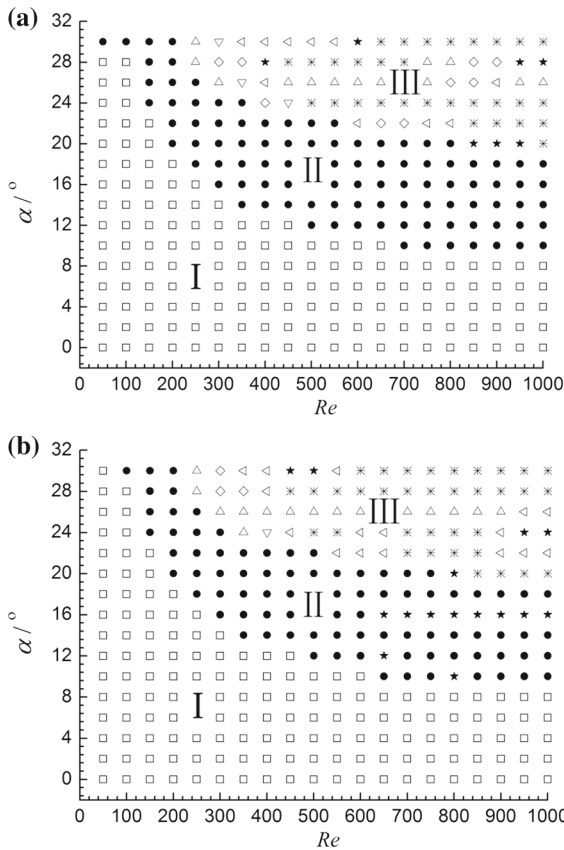
Fig. 13 Schematic of the vibration states at the membrane center at $Eh = 100$ and different pre-strains: **a** $\delta_0 = 0.01$; **b** $\delta_0 = 0.02$. I represents the static region, II period 1 vibrating region, and III complicated region. Square represents the static state, filled circle: period 1, open triangle: period 2, down triangle: period 3, diamond: period 4, left triangle: multiple period (with period larger than four), star: quasiperiod, and asterisks: chaos

unsteady responses at $\alpha = 0°$ are suppressed, as shown in Fig. 13a, b. Second, similar with that in Fig. 10, the VIV states of some points in region II, most of which are also in $700 \le Re \le 1000$ and $14° \le \alpha \le 16°$, are changed significantly when the pre-strain is increased from 0 to 0.02. Figures 14 and 15 display the phase portraits and spectrograms and the transient streamlines at $Re = 900$, $\alpha = 16°$, $Eh = 100$ and $\delta_0 = 0.01$ and 0.02, respectively. Comparing Fig. 15b with Figs. 12a and 15a, it can be found that the scale of the secondary vortices near the leading edge is increased at $\delta_0 = 0.02$, which is also believed to be the reason for the quasiperiod response at $\delta_0 = 0.02$, as shown in Fig. 14b.

5 Conclusions

Dynamic responses of a fixed 2D PR membrane wing at $0 < Re \le 1000$ and $0° \le \alpha \le 30°$ are investigated using a well-validated FSI solution procedure based on a modified CBS FEM, and the bifurcation characteristics of the VIV state with respect to the Reynolds number and angle of attack as well as their relationship with the changes of the vortex structures in the flow flied are discussed in detail. Based on the numerical results obtained, several conclusions could be made as follows:

1. At $0 < Re \le 1000$ and $0° \le \alpha \le 30°$, the 2D PR membrane wing could exhibit various VIV states, such as the bi-stable state, static state, period 1, period 2, period 3, period 4, multiple period, quasiperiod and chaos. With increase in the Reynolds number and/or angle of attack, the dynamic response will transfer first from static state to period 1 via Hopf bifurcation and then from period 1 to period 2, period 4, multiple period and chaos via a succession of period-doubling bifurcations.
2. The transient flow fields show that the Hopf bifurcation of the VIV of the membrane wing is triggered by the shedding of the leading- and/or trailing-edge vortices, while the period-doubling bifurcations are caused by the appearance and evolution of the secondary vortices. At $Re \le 1000$, perturbations from the secondary vortices play the key role in the instability of the periodic response of a membrane wing. This is very different from that at $Re = 10^3 \sim 10^4$, in which the shedding of the LEVs is the key reason for the destroy of the period 1 response [17].
3. With the increase in the structure rigidity or pre-strain, the boundary of Hopf bifurcation in the $Re - \alpha$ plane is almost unchanged, but the region III with complicated response is enlarged slightly. Moreover, dynamic responses of the membrane wing near $14° \le \alpha \le 16°$ and $700 \le Re \le 1000$ are found more sensitive to the change of rigidity or pre-strain. With the increase in rigidity or pre-strain, the period 1 response will turn to period 3, period 4, quasiperiod or chaos due to the change of the shedding process of the LEVs caused by the decrease in the mean camber. In addition, it

Fig. 14 Phase portraits and spectrograms at $Re = 900$, $\alpha = 16°$ and $Eh = 100$: **a** $\delta_0 = 0.01$; **b** $\delta_0 = 0.02$
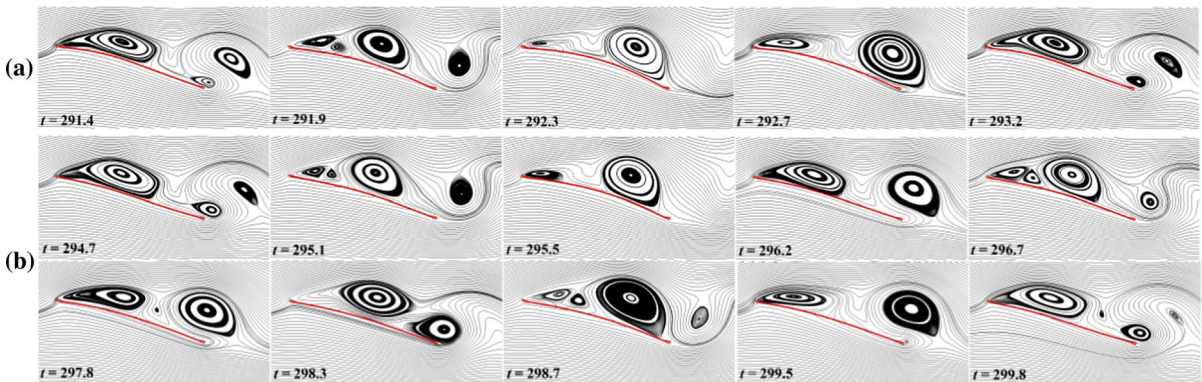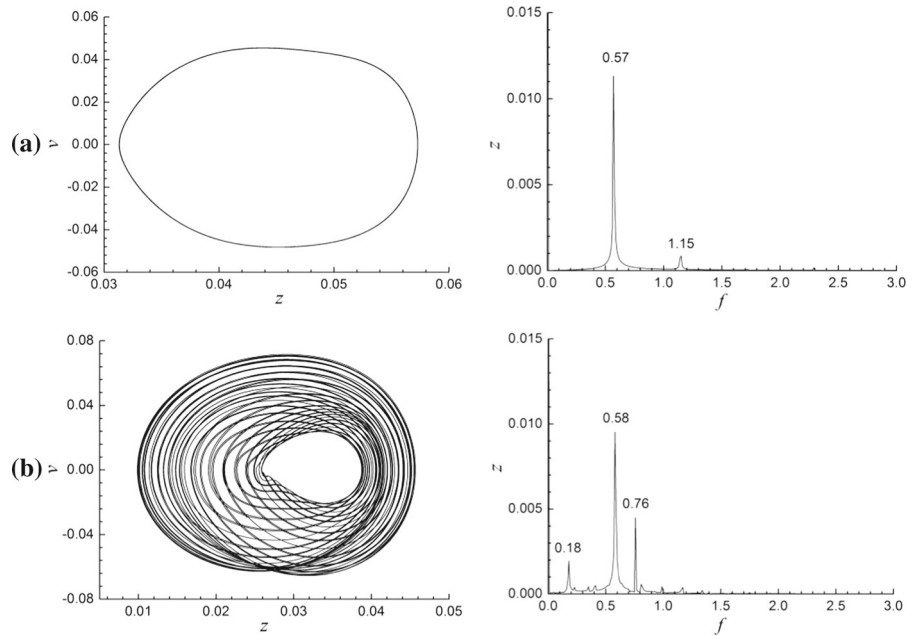

Fig. 15 Transient streamlines around the membrane wing at $Re = 900$, $\alpha = 16°$ and $Eh = 100$: **a** $\delta_0 = 0.01$; **b** $\delta_0 = 0.02$

is also found that small pre-strain will suppress the VIVs of the 2D PR membrane wing at $\alpha = 0°$.

References

1. Lian, Y.S., Shyy, W., Viieru, D., Zhang, B.N.: Membrane wing aerodynamics for micro air vehicles. Prog. Aerosp. Sci. **39**, 425–465 (2003)

2. Stanford, B., Ifju, P., Albertani, R., Shyy, W.: Fixed membrane wings for micro air vehicles: experimental characterisation, numerical modelling and tailoring. Prog. Aerosp. Sci. **46**, 258–294 (2008)

3. Shyy, W., Ifju, P., Viieru, D.: Membrane wing-based micro air vehicles. Appl. Mech. Rev. **58**, 203–301 (2005)

4. Shyy, W., Aono, H., Chimakurthi, S.K., Trizila, P., Kang, C.-K., Cesnik, C.E.S., Liu, H.: Recent progress in flapping wing aerodynamics and aeroelasticity. Prog. Aerosp. Sci. **46**, 284–327 (2010)

5. Gursul, I., Cleaver, D.J., Wang, Z.: Control of low Reynolds number flows by means of fluid–structure interactions. Prog. Aerosp. Sci. **64**, 17–55 (2014)

6. Albertani, R., Stanford, B., Hubner, Jp, Ifju, P.G.: Aerodynamic coefficients and deformation measurements on flexible micro air vehicle wings. Exp. Mech. **47**, 625–635 (2007)

7. Song, A., Tian, X.D., Israeli, E., Galvao, R., Bishop, K., Swartz, S., Breuer, K.: Aeromechanics of membrane wings with implications for animal flight. AIAA J. **46**(8), 2096–2106 (2008)

8. Gordnier, R.E.: High fidelity computational simulations of a membrane wing airfoil. J. Fluid Struct. **25**, 897–917 (2009)

9. Gordnier, R.E., Attar, P.J.: Impact of flexibility on the aerodynamics of an aspect ratio two membrane wing. J. Fluid Struct. **45**, 138–152 (2014)

10. Bleischwitz, R., de Kat, R., Ganapathisubramani, B.: Aspect-ratio effects on aeromechanics of membrane wings at moderate Reynolds numbers. AIAA J. **53**(3), 780–788 (2015)

11. Zhang, Z., Martin, N., Wrist, A., Hubner, J.P.: Geometry and prestrain effects on the aerodynamic characteristics of batten-reinforced membrane wings. J. Aircraft **53**, 530–544 (2016)

12. Rojratsirikul, P., Wang, Z., Gursul, I.: Unsteady aerodynamics of membrane airfoils. In: AIAA Paper 2008-0613 (2008)

13. Rojratsirikul, P., Wang, Z., Gursul, I.: Unsteady fluid–structure interactions of membrane airfoils at low Reynolds numbers. Exp. Fluids **46**(5), 859–72 (2009)

14. Rojratsirikul, P., Wang, Z., Gursul, I.: Effect of pre-strain and excess length on unsteady fluid–structure interactions of membrane airfoils. J. Fluid Struct. **18**(3), 359–376 (2010)

15. Rojratsirikul, P., Genc, M., Wang, Z., Gursul, I.: Flow-induced vibrations of low aspect ratio rectangular membrane wings. J. Fluid Struct. **19**, 1296–1309 (2011)

16. Galvao, R., Israeli, E., Song, A., Tian, X.D., Bishop, K., Swartz, S., Breuer, K.: The aerodynamics of compliant membrane wings modelled on mammalian flight mechanics. In: AIAA Paper, 2866, p. 2006 (2006)

17. Sun, X., Ren, X.L., Zhang, J.Z.: Nonlinear dynamic responses of a perimeter-reinforced membrane wing in laminar flows. Nonlinear Dyn. **88**(1), 749–776 (2017)

18. Smith, R., Shyy, W.: Computation of unsteady laminar flow over a flexible two-dimensional membrane wing. Phys. Fluids **7**, 2175 (1995)

19. Smith, R., Shyy, W.: Computation of aerodynamic coefficients for a flexible membrane airfoil in turbulent flow: a comparison with classical theory. Phys. Fluids **8**, 3346 (1996)

20. Sun, X., Zhang, J.Z.: Finite-element analysis of nonlinear fluid-membrane interactions using a modified characteristic-based split (CBS) scheme. In: Afraimovich, V., Machado, J.A.T., Zhang, J.Z. (eds) Complex Motions and Chaos (Springer, Switzerland, 2016), Chap. 3, p. 75

21. Sun, X., Zhang, J.Z.: Effect of the reinforced leading or trailing edge on the aerodynamic performance of a perimeter-reinforced membrane wing. J. Fluid Struct. **68**, 90–112 (2017)

22. Sun, X., Zhang, J.Z., Ren, X.L.: Characteristic-based split (CBS) finite element method for incompressible viscous flow with moving boundaries. Eng. Appl. Comput. Fluid Mech. **6**(3), 461–474 (2012)

23. Sun, X., Zhang, J.Z., Mei, G.H.: An Improved characteristic-based split (CBS) scheme for compressible and incompressible moving boundary flows. Int. J. Aerosp. Lightweight Struct. **2**(2), 281–297 (2012)

24. Blom, F.J.: Considerations on the spring analogy. Int. J. Numer. Methods Fluids **32**(6), 647–668 (2000)

25. Jameson, J.: Time dependent calculations using multigrid with application to unsteady flows past airfoils and wings. In: AIAA paper 91-1596 (1991)

26. Chung, J., Hulbert, G.: A time integration algorithm for structural dynamics with improved numerical dissipation: the generalized-α method. J. Appl. Mech. **60**(2), 371–375 (1993)

27. Sun, X., Zhang, J.Z.: Nonlinear vibrations of a flexible membrane under periodic load. Nonlinear Dyn. **85**, 2467–2486 (2016)

28. Zienkiewicz, O.C., Taylor, R.L., Nithiarasu, P.: The Finite Element Method for Fluid Dynamics, six edn. Elsevier, Butterworth (2005)